Observation of Protected Photonic Edge States Induced by Real-Space Topological Lattice Defects

Qiang Wang[1], Haoran Xue[1], Baile Zhang[1,2,*] and Y. D. Chong[1,2,†]

[1]*Division of Physics and Applied Physics, School of Physical and Mathematical Sciences, Nanyang Technological University, Singapore 637371, Singapore*
[2]*Centre for Disruptive Photonic Technologies, Nanyang Technological University, Singapore 637371, Singapore*

Topological defects (TDs) in crystal lattices are elementary lattice imperfections that cannot be removed by local perturbations, due to their real-space topology. In the emerging field of topological photonics, photonic topological edge states arise from the nontrivial topology of the band structure defined in momentum space and are generally protected against defects. Here we show that adding TDs into a valley photonic crystal generates a lattice disclination that acts like a domain wall and hosts photonic topological edge states. Unlike previous topological waveguides, the disclination forms an open arc and functions as a free-form waveguide connecting a pair of TDs of opposite topological charge. This interplay between the real-space topology of lattice defects and momentum-space band topology provides a novel scheme to implement large-scale photonic structures with complex arrangements of robust topological waveguides and resonators.

Introduction.—The emerging field of topological photonics [1] seeks to use ideas from topological band theory [2] to realize photonic modes such as edge states that are protected against defects or disorder. Valley photonic crystals (VPCs) [3–11] and photonic crystals based on topological crystalline insulators [12–15] are promising platforms because they can be implemented entirely with dielectrics or metals. Their applications are still being explored, including robust waveguides and optical delay lines [5,8,10,11,16–20], frequency converters [21,22], and lasers [23–28]. The bulk-edge correspondence principle states that topological photonic edge states are tied to the nontrivial topology of the underlying bulk band structure, as defined in momentum space; hence, they are robust against real-space defects in the lattice structure.

Topological defects (TDs) in crystal lattices are lattice imperfections that cannot be removed by local perturbations due to their real-space topological features [29]. In condensed matter, TDs are responsible for many interesting effects, including acting as seeds of disorder in the melting of two-dimensional (2D) solids [30]. Honeycomb lattices, like the 2D material graphene, can host a special class of TDs consisting of five- and seven-membered rings, which act upon 2D Dirac cone states like singular gauge fields carrying $\pi/2$ flux [31–35]. Experimental evidence for these intriguing electronic features has been difficult to obtain, due in part to challenges in sample preparation [34,36–39]. It is known that photonic structures can realize lattice phenomena that are hard to obtain in condensed matter settings; for example, "photonic graphene" has been shown to exhibit unconventional edge states that are difficult to stabilize in graphene [40]. The aforementioned physical effects of TDs, however, have yet to be explored with photonics.

Here, we present a theoretical and experimental study of an interesting form of topologically protected waveguiding aided by TDs in VPCs. VPCs are photonic analogs of valleytronic materials [41], such as honeycomb photonic crystals with broken sublattice symmetry, whose band structures contain valleys with different topological charges. In such lattices, TDs are the terminal points for disclinations—stringlike lattice defects—that cannot be gauged away [35,42]. The disclinations are locally equivalent to valley Hall domain walls [3,5,6] and act as robust topological waveguides [1].

TDs supply a novel and interesting relationship between topological features and edge states distinct from the usual bulk-edge correspondence principle. TDs carry topological charges in real space that stem from the configuration of the lattice, not band structure features defined in momentum space. Positive and negative TDs are joined pairwise by disclinations hosting edge states, but unlike standard VPC domain walls one can go smoothly from one domain to the other by encircling a TD without crossing the disclination. This feature requires the presence of TDs and does not occur in perfect crystals. The disclinations can follow curved paths and are not restricted to any global axes [3,6]. They are also not limited to forming loops or ending at external boundaries and can form open arcs (bounded by the TDs) that act as one-dimensional (1D) Fabry-Perot resonators based on counterpropagating topological edge states.

Previous research has shown that amorphous photonic structures, which possess short-range positional order without long-range order, can exhibit isotropic photonic band gaps, making them suitable for inscribing with free-form curved waveguides [43–49]. A key limitation of such waveguides is that, as irregular 1D transport channels, they are highly susceptible to Anderson localization [50]; for long-range transport, it becomes necessary to perform structural fine-tuning to optimize the transmittance [49]. We show that the present disclination-based topological waveguides have much greater resistance against Anderson localization without structural fine-tuning [1,3]. Moreover, unlike earlier demonstrations of topological waveguiding in amorphous or quasicrystalline lattices [51,52], the present design does not require time-reversal symmetry breaking.

Setup.—Consider the honeycomb lattice shown in Fig. 1(a). Red and blue circles represent sites on the two sublattices A and B. By deleting a $\pi/3$ sector (marked by dashes) and reattaching the seams, a pentagonal TD is generated [31], as shown in Fig. 1(b). Likewise, inserting a $\pi/3$ sector yields a heptagonal TD, as shown in Fig. 1(c). Each TD is attached to a disclination of bonds that join sites of the same sublattice, as indicated by dashes in Figs. 1(b) and 1(c). If the A and B sites are identical, the disclination is fictitious: one end is p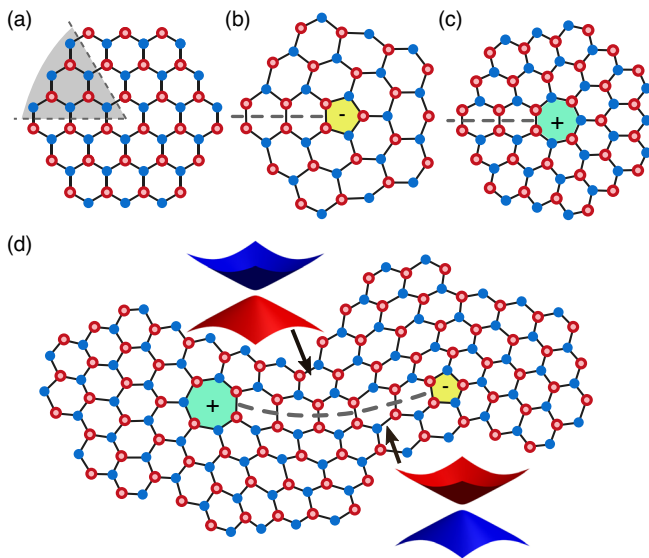inned to the TD but the rest of it can be moved around by adjusting the assignment of sites to the A and B sublattices. In the continuum limit, the states of the honeycomb lattice are described by a pair of Dirac cones, and the disclination is associated with a nontrivial boundary condition for the Dirac cone states, which can be transformed into a regular continuity condition (i.e., gauged away) using a matrix-valued gauge field [31,32,42,53]. The qualitative features of these lattice configurations can be studied with tight-binding models; if we assign on site energies (or frequency detunings [54]) of $m_A = -m_B = m$ to the A and B sites, then there is a bulk band gap in the energy range $m_B < E < m_A$. For $m \neq 0$, the disclination is physical and cannot be gauged away [42], and the bulk gap is populated by eigenstates localized on the disclination (see the Supplemental Material [55]). The similarity of the disclination to domain walls in valley Hall (VH) lattices, which likewise consist of strings of nearest-neighbor sites of the same sublattice, indicates that these are VH-like topological edges. However, whereas a VH domain wall can only form a loop or terminate at exterior lattice edges, the disclination can terminate within the bulk, at the TD. A theoretical analysis confirms that Dirac cone states experience the disclination as a VH-like domain wall, across which the Dirac mass of each valley switches sign [55].

We performed a series of experimental studies of disclination-bound photonic states in microwave-scale VPCs, formed by dielectric pillars sandwiched between parallel metal plates. Samples with one pentagonal TD at the center are shown in Figs. 2(a) and 2(d). The lattices are generated by starting with a $2\pi/5$ or $2\pi/7$ sector, populating with an unoptimized triangular lattice and close packing the sites with the molecular dynamics simulator LAMMPS [55,56]. The other sectors are determined by fivefold rotational symmetry, and a dual lattice is generated by treating the triangular lattice sites as honeycomb motif incenters [57]. The dielectric pillars have refractive index $n = 2.915$, height $h_1 = 10$ mm, and radius $r_a = 2.35$ mm (for A sites) or $r_b = 3.15$ mm (for B sites). The lattices are scaled so the mean next-nearest-neighbor distance is $a = 13.7$ mm. By assigning sites to the A or B sublattice, we can set the path of the disclination emanating from the TD, including introducing sharp corners. Figures 2(a)–2(c) and 2(d)–2(f) correspond to two different disclinations.

Figures 2(b) and 2(e) show the experimentally measured intensity profiles for transverse magnetic waves emitted by a dipole source placed at the TD, oriented perpendicular to the plane. The excitation frequency of 7.72 GHz lies within the bulk band gap calculated for a perfectly crystalline VPC (see the Supplemental Material [55]). The waves emitted by the dipole are guided along the disclination, including around a sharp corner in Fig. 2(e). Figures 2(c) and 2(f) show the frequency dependence of the experimentally measured field intensities sampled over the disclination or in the bulk. Over the frequencies of the bulk gap, we observe a clear intensity dip in the bulk, but no dip on the disclination.

FIG. 1. Valley hall lattices with TDs. (a) Defect-free honeycomb lattice with red (blue) circles indicating sites on sublattice A (B) and black lines indicating nearest-neighbor bonds. The gray region bounded by dashes marks a $\pi/3$ sector whose deletion generates a pentagonal TD. (b),(c) Lattice containing a pentagonal TD (labeled $-$) or heptagonal TD (labeled $+$) and a disclination (dashes) comprising a string of bonds joining sites on the same sublattice. (d) Lattice with one pentagonal TD and one heptagonal TD, connected by a disclination forming an open arc.
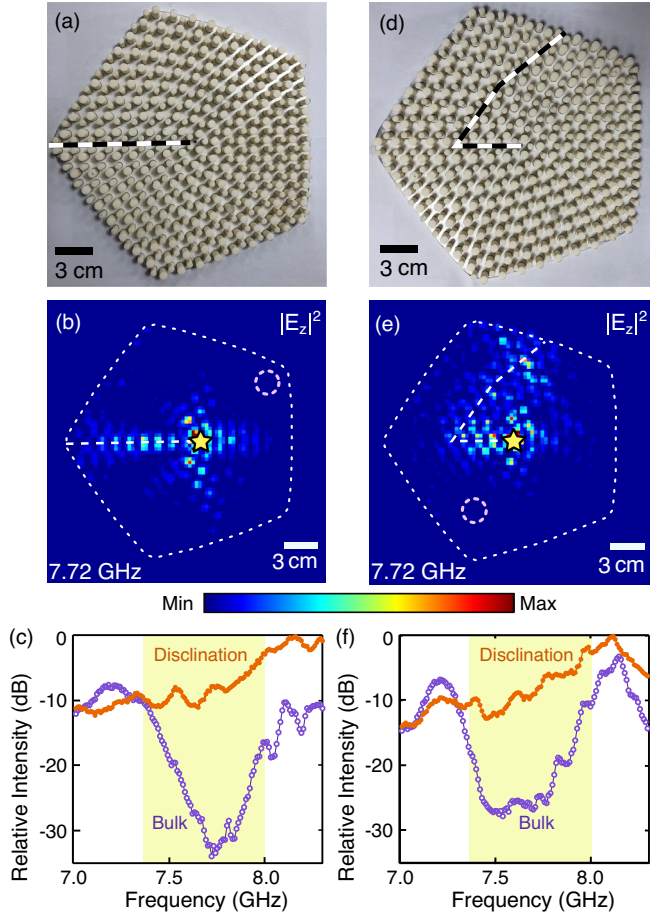
FIG. 2. Experimental study of VPCs with pentagonal TDs. (a) Photograph of VPC with top plate removed. The external region is an empty parallel plate waveguide with 11 mm spacing (i.e., 1 mm air gap between the moving top plate and the pillars). The lattice contains a pentagonal TD, with a disclination marked by dashes. (b) Measured distribution of the electric field intensity ($|E_z|^2$) produced by a dipole source at the TD (yellow star). The dots indicate the sample boundary. The scanning resolution is 3×3 mm. (c) Frequency spectrum of $|E_z|^2$ averaged over the disclination (orange points) or in the bulk (purple points). The disclination sampling region is a thin (3 mm wide) strip running along the disclination; the bulk sampling region is the circle shown in (b). The bulk band gap predicted from full-wave simulations is marked in yellow. The intensities are normalized to the maximum intensity for the disclination measurements. (d)–(f) Corresponding results for a disclination containing a sharp bend.

We used full-wave eigenmode calculations to verify that these transmission characteristics are attributable to eigenmodes localized along the disclination [55]. The number of eigenmodes and their eigenfrequencies depend on the size of the lattice and also on the details of the packing procedure used to generate the lattice; in the experiments, we use settings that ensure a low level of variation in the spacings between different nearest-neighbor sites. Further details about the experimental setup,

and the accompanying simulations, are given in the Supplemental Material [55].

For comparison, we also investigated a photonic graphene lattice with all pillars having the same radius. According to previous theoretical studies, TDs in such lattices do not create localized resonances [32,42,53], and there are no disclinations hosting edge states. This is corroborated by our experimental results (see the Supplemental Material [55]).

Waveguiding with and without TDs.—Turning now to more complex VPC structures, we implemented large-scale VPCs hosting topological and nontopological waveguides. As shown in Figs. 3(a)–3(c), each waveguide forms an open arc following a straight path, a curved path, or a curved path containing a sharp bend, based on a disclination connecting a pentagonal and heptagonal TD. We use a similar lattice generation procedure (starting from an unoptimized lattice with the desired TDs, close packing, and conversion to a dual honeycomblike lattice) and the same VPC parameters as before. In Figs. 3(a)–3(c), we plot the results of full-wave simulations showing the field distributions produced by a dipole source at one TD. For all three configurations, the intensity distribution is roughly uniform along the entire open arc of the disclination. The waveguides thus act like 1D Fabry-Perot-like optical cavities, with the TDs serving as end mirrors (i.e., the waveguide modes experience complete intervalley scattering and backreflection at these points). There is evidently negligible Anderson localization and negligible backscattering at the sharp bend in Fig. 3(c).

For comparison, we also implemented conventional (nontopological) waveguides in similar photonic lattices, using the same bulk VPC parameters (i.e., the same pillar radii and mean interpillar spacings) but without TDs. These waveguides do not run along disclinations, but are formed by selectively removing pillars along a desired route. In a perfectly crystalline lattice, band structure calculations show that the pillar removal creates a band of defect modes over 6.77–7.05 GHz (not spanning the gap). Simulations show that the defect modes transmit efficiently when the waveguide follows a straight line [Fig. 3(e)], but suffer from localization when the route is curved [Fig. 3(f)], and do not guide light efficiently around sharp corners [Fig. 3(g)].

We implemented these six photonic structures and measured the transmission along the waveguides. The experimental results are shown in Figs. 3(d) and 3(h). The three topological waveguides (straight, curved, and sharply bent) all transmit efficiently between the waveguide endpoints, with approximately the same transmittance over 6.8–7.2 GHz. This is a narrower range than the 6.45–7.35 GHz gap predicted by simulations, which can be ascribed to intrinsic losses in the ceramic material and frequency-dependent input and output impedances. The conventional waveguides transmit with markedly lower
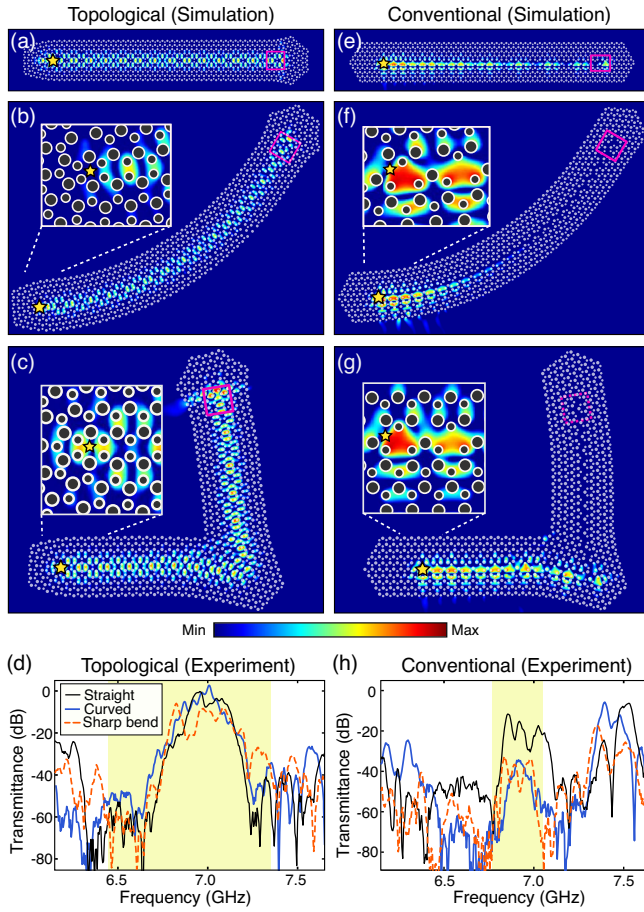
Topological (Simulation) — Conventional (Simulation)

FIG. 3. (a)–(c) Simulated field distributions for topological waveguides following a (a) straight, (b) curved, or (c) sharply bent disclination. A 6.98 GHz dipole source is placed near a TD at one end of the disclination (yellow star). Colors correspond to $\log |E_z|^2$, with all three plots normalized to the maximum intensity along waveguide (a). (d) Experimentally measured transmittance spectrum for the topological waveguides of (a)–(c). Source and probe antennas are placed at each end of the waveguide, and results are normalized to the maximum transmittance on the straight topological waveguide. Here, the parallel plates have 10 mm spacing (i.e., no air gap), which shifts the band gap relative to Fig. 2 (see the Supplemental Material [55]). (e)–(g) Simulated field distributions ($\log |E_z|^2$) for nontopological waveguides generated by removing pillars from VPCs without TDs. A 6.98 GHz dipole source is placed near one end (yellow star). All three plots are normalized to the maximum intensity on waveguide (d). (h) Experimentally measured transmittance spectrum for the nontopological waveguides (e)–(g), normalized to the maximum transmittance on the straight topological waveguide in (d). In (d) and (h), the operating frequency ranges predicted by simulations are marked in yellow.

efficiency; the bent and curved routes have transmittances around 20 dB lower than the straight version and over 25 dB lower than the topological waveguides.

We performed field-mapping experiments on a curved topological waveguide, with results shown in Fig. 4(a). Strong field intensities are observed along the entire length
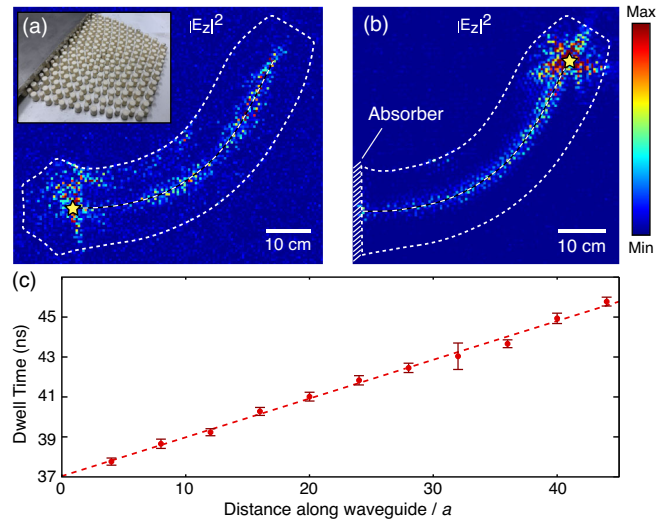

FIG. 4. (a) Experimentally measured electric field intensity distribution ($|E_z|^2$) for a curved topological waveguide running between a pentagonal TD and a heptagonal TD. A 7.66 GHz dipole source is placed near the pentagonal TD (yellow star). The scanning resolution is 5 mm × 5 mm. Inset: photograph of the sample with top plate partially retracted. (b) Measured electric field intensity distribution at 7.55 GHz for a waveguide terminating at a boundary with microwave absorbers. (c) Measured dwell times for the sample in (b), plotted against distance (arc length) along the waveguide. Each data point is the mean of 61 dwell time estimates obtained from the phase of E_z measured over a frequency range centered at 7.6 GHz with 0.002 GHz spacing. Error bars indicate the standard error of the mean, and dashes show the linear least squares fit.

of the waveguide, in agreement with the simulation results presented above. To test the propagation characteristics of the waveguide modes, we studied a sample with the curved topological waveguide terminating at a boundary lined with microwave-absorbing foam, rather than a TD. With back-reflection suppressed, this waveguide only supports waves traveling in one direction, away from the source. The experimental field intensity map is shown in Fig. 4(b). From the results, we determined the dwell time, defined as $d\varphi/d\omega$, where φ is the phase of the measured field and ω is the angular frequency [58]. To estimate the derivative, we approximate the derivative using a finite frequency spacing $df = 0.002$ GHz. We took data at different positions along the waveguide, with each data point incorporating 61 dwell time estimates centered around frequency 7.6 GHz (near the center of the gap). The resulting mean dwell time and the standard error of the mean are shown in Fig. 4(c). The dwell time scales linearly with distance (arc length) along the waveguide, consistent with ballistic propagation [58].

Discussion.—We have demonstrated that TD-induced disclinations in VPCs provide a way to implement complex large-scale photonic structures, by placing TDs at the desired end points and adjusting the disclinations to follow the desired waveguide routes. The waveguides enjoy much

greater resistance to backscattering than free-form waveguides in amorphous photonic lattices designed without topological principles [48,49]. Though originally implemented at microwave frequencies, this all-dielectric design can be scaled to higher frequencies, as shown by the recent implementation of optical and terahertz-scale VPCs [8,10,59]. From a fundamental point of view, we have demonstrated a new interplay between the real-space topology of a lattice and the momentum-space topology of Bloch wave functions, different from the previously known topological bulk-edge correspondence principle. This makes the presence of TDs in 2D honeycomb lattices, previously a subtle effect, now easily observable. In the future, it will be interesting to investigate TDs and disclinations in other types of photonic lattices, such as higher-order topological insulators [60], as well as experimentally accessing other phenomena associated with TDs, such as anomalous Aharanov-Bohm effects and localized zero modes [31–36,42,53,61–66].

---

[*] blzhang@ntu.edu.sg

[†] yidong@ntu.edu.sg

[1] T. Ozawa, H. M. Price, A. Amo, N. Goldman, M. Hafezi, L. Lu, M. C. Rechtsman, D. Schuster, J. Simon, O. Zilberberg, and I. Carusotto, Rev. Mod. Phys. **91**, 015006 (2019).

[2] A. Bansil, H. Lin, and T. Das, Rev. Mod. Phys. **88**, 021004 (2016).

[3] T. Ma and G. Shvets, New J. Phys. **18**, 025012 (2016).

[4] X. Wu, Y. Meng, J. Tian, Y. Huang, H. Xiang, D. Han, and W. Wen, Nat. Commun. **8**, 1304 (2017).

[5] J.-W. Dong, X.-D. Chen, H. Zhu, Y. Wang, and X. Zhang, Nat. Mater. **16**, 298 (2017).

[6] F. Gao, H. Xue, Z. Yang, K. Lai, Y. Yu, X. Lin, Y. Chong, G. Shvets, and B. Zhang, Nat. Phys. **14**, 140 (2018).

[7] J. Noh, S. Huang, K. P. Chen, and M. C. Rechtsman, Phys. Rev. Lett. **120**, 063902 (2018).

[8] M. I. Shalaev, W. Walasik, A. Tsukernik, Y. Xu, and N. M. Litchinitser, Nat. Nanotechnol. **14**, 31 (2019).

[9] X.-T. He, E.-T. Liang, J.-J. Yuan, H.-Y. Qiu, X.-D. Chen, F.-L. Zhao, and J.-W. Dong, Nat. Commun. **10**, 872 (2019).

[10] Y. Zeng, U. Chattopadhyay, B. Zhu, B. Qiang, J. Li, Y. Jin, L. Li, A. G. Davies, E. H. Linfield, B. Zhang, Y. Chong, and Q. J. Wang, Nature (London) **578**, 246 (2020).

[11] B. Yang, H. Zhang, T. Wu, R. Dong, X. Yan, and X. Zhang, Phys. Rev. B **99**, 045307 (2019).

[12] L.-H. Wu and X. Hu, Phys. Rev. Lett. **114**, 223901 (2015).

[13] Y. Yang, Y. F. Xu, T. Xu, H.-X. Wang, J.-H. Jiang, X. Hu, and Z. H. Hang, Phys. Rev. Lett. **120**, 217401 (2018).

[14] S. Barik, A. Karasahin, C. Flower, T. Cai, H. Miyake, W. DeGottardi, M. Hafezi, and E. Waks, Science **359**, 666 (2018).

[15] N. Parappurath, F. Alpeggiani, L. Kuipers, and E. Verhagen, Sci. Adv. **6**, eaaw4137 (2020).

[16] Z. Wang, Y. D. Chong, J. D. Joannopoulos, and M. Soljačić, Phys. Rev. Lett. **100**, 013905 (2008).

[17] Z. Wang, Y. Chong, J. D. Joannopoulos, and M. Soljai, Nature (London) **461**, 772 (2009).

[18] M. Hafezi, E. A. Demler, M. D. Lukin, and J. M. Taylor, Nat. Phys. **7**, 907 (2011).

[19] A. B. Khanikaev, S. H. Mousavi, W.-K. Tse, M. Kargarian, A. H. MacDonald, and G. Shvets, Nat. Mater. **12**, 233 (2013).

[20] W.-J. Chen, S.-J. Jiang, X.-D. Chen, B. Zhu, L. Zhou, J.-W. Dong, and C. T. Chan, Nat. Commun. **5**, 5782 (2014).

[21] Y. Hadad, J. C. Soric, A. B. Khanikaev, and A. Al, Nature Electronics **1**, 178 (2018).

[22] Y. Wang, L.-J. Lang, C. H. Lee, B. Zhang, and Y. D. Chong, Nat. Commun. **10**, 1102 (2019).

[23] P. St-Jean, V. Goblot, E. Galopin, A. Lematre, T. Ozawa, L. Le Gratiet, I. Sagnes, J. Bloch, and A. Amo, Nat. Photonics **11**, 651 (2017).

[24] H. Zhao, P. Miao, M. H. Teimourpour, S. Malzard, R. El-Ganainy, H. Schomerus, and L. Feng, Nat. Commun. **9**, 981 (2018).

[25] M. Parto, S. Wittek, H. Hodaei, G. Harari, M. A. Bandres, J. Ren, M. C. Rechtsman, M. Segev, D. N. Christodoulides, and M. Khajavikhan, Phys. Rev. Lett. **120**, 113901 (2018).

[26] Y. Ota, R. Katsumi, K. Watanabe, S. Iwamoto, and Y. Arakawa, Commun. Phys. **1**, 86 (2018).

[27] M. A. Bandres, S. Wittek, G. Harari, M. Parto, J. Ren, M. Segev, D. N. Christodoulides, and M. Khajavikhan, Science **359**, eaar4005 (2018).

[28] G. Harari, M. A. Bandres, Y. Lumer, M. C. Rechtsman, Y. D. Chong, M. Khajavikhan, D. N. Christodoulides, and M. Segev, Science **359**, eaar4003 (2018).

[29] N. D. Mermin, Rev. Mod. Phys. **51**, 591 (1979).

[30] J. M. Kosterlitz, Rev. Mod. Phys. **89**, 040501 (2017).

[31] J. González, F. Guinea, and M. A. H. Vozmediano, Nucl. Phys. **B406**, 771 (1993).

[32] P. E. Lammert and V. H. Crespi, Phys. Rev. Lett. **85**, 5190 (2000).

[33] M. A. H. Vozmediano, M. I. Katsnelson, and F. Guinea, Phys. Rep. **496**, 109 (2010).

[34] J. Kotakoski, A. V. Krasheninnikov, U. Kaiser, and J. C. Meyer, Phys. Rev. Lett. **106**, 105505 (2011).

[35] J. de Souza, C. de Lima Ribeiro, and C. Furtado, Phys. Lett. A **378**, 2317 (2014).

[36] O. V. Yazyev and S. G. Louie, Nat. Mater. **9**, 806 (2010).

[37] J. Lahiri, Y. Lin, P. Bozkurt, I. I. Oleynik, and M. Batzill, Nat. Nanotechnol. **5**, 326 (2010).

[38] P. Y. Huang, C. S. Ruiz-Vargas, A. M. van der Zande, W. S. Whitney, M. P. Levendorf, J. W. Kevek, S. Garg, J. S. Alden, C. J. Hustedt, Y. Zhu, J. Park, P. L. McEuen, and D. A. Muller, Nature (London) **469**, 389 (2011).

[39] J. H. Warner, E. R. Margine, M. Mukai, A. W. Robertson, F. Giustino, and A. I. Kirkland, Science **337**, 209 (2012).

[40] Y. Plotnik, M. C. Rechtsman, D. Song, M. Heinrich, J. M. Zeuner, S. Nolte, Y. Lumer, N. Malkova, J. Xu, A. Szameit et al., Nat. Mater. **13**, 57 (2014).

[41] D. Xiao, W. Yao, and Q. Niu, Phys. Rev. Lett. **99**, 236809 (2007).

[42] A. Rüegg and C. Lin, Phys. Rev. Lett. **110,** 046401 (2013).

[43] H. Miyazaki, M. Hase, H. T. Miyazaki, Y. Kurokawa, and N. Shinya, Phys. Rev. B **67,** 235109 (2003).

[44] K. Edagawa, S. Kanoko, and M. Notomi, Phys. Rev. Lett. **100,** 013901 (2008).

[45] M. Florescu, S. Torquato, and P. J. Steinhardt, Proc. Natl. Acad. Sci. U.S.A. **106,** 20658 (2009).

[46] J.-K. Yang, C. Schreck, H. Noh, S.-F. Liew, M. I. Guy, C. S. O'Hern, and H. Cao, Phys. Rev. A **82,** 053838 (2010).

[47] S. Imagawa, K. Edagawa, K. Morita, T. Niino, Y. Kagawa, and M. Notomi, Phys. Rev. B **82,** 115116 (2010).

[48] W. Man, M. Florescu, E. P. Williamson, Y. He, S. R. Hashemizad, B. Y. C. Leung, D. R. Liner, S. Torquato, P. M. Chaikin, and P. J. Steinhardt, Proc. Natl. Acad. Sci. U.S.A. **110,** 15886 (2013).

[49] M. Florescu, P. J. Steinhardt, and S. Torquato, Phys. Rev. B **87,** 165116 (2013).

[50] B. Kramer and A. MacKinnon, Rep. Prog. Phys. **56,** 1469 (1993).

[51] M. A. Bandres, M. C. Rechtsman, and M. Segev, Phys. Rev. X **6,** 011016 (2016).

[52] N. P. Mitchell, L. M. Nash, D. Hexner, A. M. Turner, and W. T. M. Irvine, Nat. Phys. **14,** 380 (2018).

[53] P. E. Lammert and V. H. Crespi, Phys. Rev. B **69,** 035406 (2004).

[54] W. Suh, Z. Wang, and S. Fan, IEEE J. Quantum Electron. **40,** 1511 (2004).

[55] See Supplemental Material at http://link.aps.org/supplemental/10.1103/PhysRevLett.124.243602 for effects of topological defects on Dirac cone states, numerical results for the tight-binding models, details on lattice generation, design of photonic lattice, full-wave simulation, experimental setup, and further experimental results.

[56] S. Plimpton, J. Comput. Phys. **117,** 1 (1995).

[57] S. Mansha, Y. Zeng, Q. J. Wang, and Y. D. Chong, Opt. Express **24,** 4890 (2016).

[58] X. Cheng, C. Jouvaud, X. Ni, S. H. Mousavi, A. Z. Genack, and A. B. Khanikaev, Nat. Mater. **15,** 542 (2016).

[59] Y. Yang, Y. Yamagami, X. Yu, P. Pitchappa, B. Zhang, M. Fujita, T. Nagatsuma, and R. Singh, Nat. Photonics (2020), https://doi.org/10.1038/s41566-020-0618-9.

[60] J. Noh, W. A. Benalcazar, S. Huang, M. J. Collins, K. P. Chen, T. L. Hughes, and M. C. Rechtsman, Nat. Photonics **12,** 408 (2018).

[61] Y. A. Sitenko and N. D. Vlasii, Nucl. Phys. **B787,** 241 (2007).

[62] A. Cortijo and M. A. Vozmediano, Eur. Phys. J. Special Topics **148,** 83 (2007).

[63] B. W. Jeong, J. Ihm, and G.-D. Lee, Phys. Rev. B **78,** 165403 (2008).

[64] Y. Wei, J. Wu, H. Yin, X. Shi, R. Yang, and M. Dresselhaus, Nat. Mater. **11,** 759 (2012).

[65] R.-J. Slager, J. Phys. Chem. Solids **128,** 24 (2019).

[66] T. Kariyado and R.-J. Slager, Phys. Rev. Research **1,** 032027 (2019).